Chemogenetic silencing of neurons in the mouse anterior cingulate area modulates neuronal activity and functional connectivity

Lore M. Peeters*[a], Rukun Hinz[a], Jan R. Detrez[b], Stephan Missault[a], Winnok H. De Vos[b], Marleen Verhoye[a], Annemie Van der Linden[a], Georgios A. Keliris*[a]

[a] Bio-Imaging Lab, University of Antwerp, Universiteitsplein 1 2610 Wilrijk, Belgium
[b] Laboratory for Cell Biology and Histology, University of Antwerp, Universiteitsplein 1 2610 Wilrijk, Belgium

*Corresponding authors:

Lore M. Peeters
Bio-Imaging lab, University of Antwerp
Campus Drie Eiken – Building UC 1.17
Universiteitsplein 1 – 2610 Wilrijk – Belgium
Tel. +32 2651816
e-mail: lore.peeters@uantwerpen.be

or

Georgios A. Keliris
Bio-Imaging Lab, University of Antwerp
Campus Drie Eiken – Building UC 1.17
Universiteitsplein 1 – 2610 Wilrijk – Belgium
Tel. +32 2652772
e-mail: georgios.keliris@uantwerpen.be

Keywords: Designer Receptors Exclusively Activated by Designer Drugs (DREADDs), kappa-opioid receptor DREADDs (KORD), pharmacological functional MRI, resting state functional MRI, neuronal activity, functional connectivity.

1

29   **Abstract**

30   The anterior cingulate area (ACA) is an integral part of the prefrontal cortex in mice and has been

31   implicated in several cognitive functions. Previous anatomical and functional imaging studies

32   demonstrated that the ACA is highly interconnected with numerous brain regions acting as a hub region

33   in functional networks. However, the importance of the ACA in regulating functional network activity and

34   connectivity remains to be elucidated. Recently developed neuromodulatory techniques, such as Designer

35   Receptors Exclusively Activated by Designer Drugs (DREADDs) allow for precise control of neuronal

36   activity. In this study, we used an inhibitory kappa-opioid receptor DREADDs (KORD) to temporally inhibit

37   neuronal firing in the right ACA of mice and assessed functional network activity and connectivity using

38   non-invasive functional MRI. We demonstrated that KORD-induced inhibition of the right ACA induced

39   blood oxygenation-level dependent (BOLD) signal decreases and increases in connected brain regions

40   throughout of hemispheres. Furthermore, these modulations in neuronal activity were associated with

41   decreased intra- and interhemispheric functional connectivity. These results demonstrate that the

42   combination of the DREADD technology and non-invasive functional imaging methods is a valuable tool

43   for unraveling the underlying mechanisms of network function and dysfunction.

44

45

1. Introduction

The anterior cingulate area (ACA) is an integral part of the prefrontal cortex and has been implicated in several cognitive functions including attention [1-3], remote memory [4, 5], motion planning and execution [6] and processing of pain [7]. Accumulating evidence suggests that the cytoarchitecture and functional role of the ACA is similar across different species including humans, non-human primates and rodents [8-11]. Anatomical and functional imaging studies identified the ACA as a central hub region that is highly interconnected with numerous brain regions and involved in multiple functional networks [12-14]. ACA hypoconnectivity, as measured in functional MRI studies, is associated with network dysfunctions implicated in multiple psychiatric disorders, such as attention-deficit hyperactivity disorder [15], schizophrenia [16, 17], bipolar disorder [18, 19], depression and anxiety [20]. Furthermore, abnormal functional connectivity (FC) of the ACA has also been shown to occur following traumatic brain injury [21, 22]. This implicates that the ACA is involved in a wide range of neurological disorders. Nevertheless, the direct role of neuronal populations in the ACA in maintaining neuronal network function has not yet been examined to date.

During the last decade, researchers have focused on the development of new neuromodulatory tools, such as optogenetics and chemogenetics, which allow controlling the activity of specifically targeted neuronal populations with spatiotemporal specificity. Current chemogenetic tools include Designer Receptors Exclusively Activated by Designer Drugs (DREADDs), which are engineered receptors for targeted enhancement or silencing of neurons upon binding of an otherwise inert ligand. The combination of chemogenetics and non-invasive neuroimaging methods, such as functional magnetic resonance imaging (fMRI), allows direct evaluation of DREADD-induced changes in neuronal firing on large-scale neuronal activity and FC. As such, Giorgi et al. were able to causally link the chemogenetic activation of serotonergic neurons with neuronal activity increases in cortical and subcortical brain areas, measured by relative cerebral blood volume increases [23]. Furthermore, other studies also used blood-oxygenation-

70   level-dependent (BOLD) fMRI to identify the effect of chemogenetic activation of mesolimbic and

71   mesocortical pathways [24] or chemogenetic inhibition of the amygdala [25] on whole-brain network

72   integrity.

73   Here, we combined inhibitory kappa opioid-receptor DREADDs (KORD) in the mouse ACA and non-invasive

74   fMRI in order to evaluate the link between inhibition of the ACA and whole-brain network activity and

75   connectivity. We hypothesized that acute inhibition of the ACA leads to neuronal activity and FC

76   alterations in structurally and functionally connected brain regions. Pharmacological MRI (phMRI) was

77   used to assess changes in BOLD activation levels after injection of the chemogenetic agent, Salvinorin B

78   (SalB), an inert ligand of the KORD. Changes in neuronal activity were evaluated in the target region as

79   well as in connected brain areas. Resting state fMRI (rsfMRI) was used to identify brain wide FC alterations

80   that may reflect neuronal network reorganizations and disruptions similar to disease states.

81   **2. Methods**

82   ***2.1 Animals and ethics statement***

83   Healthy male C57BL/6J mice (N = 18; Janvier, France) of (34 ± 1) g were used in the study. Animals were

84   group housed under controlled humidity (40%) and temperature (20 − 24°C) conditions, with a 12h

85   light/dark cycle. Standard food and water were provided ad libitum. All procedures were in accordance

86   with the guidelines approved by the European Ethics Committee (decree 2010/63/EU) and were approved

87   by the Committee on Animal Care and Use at the University of Antwerp, Belgium (approval number: 2016-

88   49).

89   ***2.2 Intracerebral viral vector injections***

90   Mice were subjected to a stereotactic surgery targeting the right ACA (AP +0.86 mm, ML +0.50 mm, DV -

91   0.75 mm). Mice were randomly divided into two groups: a KORD-expressing group (N=12) and a sham

92   group (N=6). Viral vector injections were performed as follows: mice were anesthetized using 2%

4

93   isoflurane (Isoflo®, Abbott Laboratories Ltd., USA) and received a subcutaneous (s.c.) injection of xylocaine

94   (Lidocaine hydrochloride, Astra Zeneca) for local analgesia. The following viral vectors were injected: 1 µL

95   of 3.3 x 10^{12} vector genomes (vg)/mL of AAV8-CaMKII-HA-KORD-IRES-mCitrine (Vector Core, University of

96   North Carolina, USA) in the KORD-expressing group, and 1 µL of 5.6 x 10^{12} vg/mL of AAV8-CaMKIIa-EGFP

97   (Vector Core, University of North Carolina, USA) in the sham group. The virus was injected at a rate of 18.3

98   nL/min with a nano-injector (Nanoject II, Drummond). The MRI experiments started at least three weeks

99   after viral vector injection to allow optimal expression levels [26].

100   ***2.3 In vivo MRI procedures***

101   Initially, mice were anesthetized with 2% isoflurane in a mixture of 70% N_2 and 30% O_2. During the imaging

102   procedures, an optimized anesthesia protocol was used [27]. Briefly, a s.c. bolus injection of 0.05 mg/kg

103   medetomidine (Domitor®, Pfizer, Germany) was administered, and after 10 min a s.c. infusion of 0.1

104   mg/kg/h medetomidine was started. Meanwhile, the isoflurane level was gradually decreased to 0.3%.

105   Functional imaging scans were acquired starting from forty minutes post-bolus injection. The animals'

106   physiology was closely monitored throughout the acquisition of the MRI scans. The breathing rate was

107   recorded using a pressure-sensitive pad (sampling rate 225 Hz; MR-compatible Small Animal Monitoring

108   and Gating system, SA Instruments, Inc., USA) and the body temperature was maintained at (37 ± 0.5) °C

109   using a feedback controlled warm air circuitry (MR-compatible Small Animal Heating System, SA

110   Instruments, Inc., USA). In addition, the level of blood oxygenation was monitored using a pulse oximeter

111   (MR-compatible Small Animal Monitoring and Gating System, SA Instruments, Inc., USA). After the

112   imaging procedures, the medetomidine anesthesia was reversed by injecting 0.1 mg/kg atipamezole

113   (Antisedan®, Pfizer, Germany).

114   All MRI scans were acquired on a 9.4T Biospec MRI system (Bruker BioSpin, Germany) with Paravision

115   6.0.1 software. The images were acquired using a standard Bruker crosscoil set-up with a quadrature

116   volume coil and a quadrature surface coil designed for mice. First, three orthogonal multi-slice Turbo RARE

5

117   T_2-weighted images were acquired to enable uniform slice-positioning (TR: 2000 ms, TE: 33 ms, matrix:

118   [256x256], FOV: (20x20) mm^2, in-plane resolution: (0.078x0.078) mm^2, 16 coronal slices of 0.4 mm). Then,

119   inhomogeneity of the magnetic field in an ellipsoidal volume of interest within the brain was corrected by

120   local shimming. The phMRI scans and rsfMRI scans were acquired during separate scan sessions.

121   **_2.4 Assessing KORD-induced neuronal activity changes_**

122   _2.4.1 MRI data Acquisition_

123   PhMRI data were acquired using a T_2^* weighted echo planar imaging (EPI) sequence (TR: 15000 ms, TE: 20

124   ms, matrix: [64x64], FOV: (20x20) mm^2, two segments, in-plane resolution: (0.312x0.312) mm^2, 16 coronal

125   slices of 0.4 mm covering cerebrum excluding olfactory bulb). Baseline scans were acquired for 10 min (20

126   volumes) after which SalB (3 mg/kg (sham and KORD group) or 6 mg/kg (KORD group); Toronto Research

127   Chemicals, Canada; dissolved in DMSO, as previously described in [26]) was administered through a s.c.

128   catheter. Following the acquisition of the ten minutes baseline scan, the scan was continued until fifty

129   minutes (100 volumes) after the SalB injection. The KORD group was scanned with different SalB

130   concentrations (3 mg/kg and 6 mg/kg, separate scan sessions) to assess concentration effects. A total of

131   three scans, two scans from the sham group and one scan from the 3 mg/kg SalB KORD group, were

132   excluded from the phMRI analysis due to signal instabilities. Final group sizes for the phMRI scans were:

133   sham group: N=4 and KORD-expressing group: 3mg/kg SalB N=11, 6 mg/kg SalB N=12.

134   _2.4.2 MRI data pre-processing_

135   Data pre-processing was performed using SPM12 software in MATLAB 2014a. Realignment and unwarping

136   were performed using a least-squares approach and a 6-parameter rigid body spatial transformation.

137   Second, all scans were normalized to the study-specific mean EPI template using a global 12-parameter

138   affine transformation, followed by a non-linear transformation. Then, in-plane smoothing was performed

139   on masked images with a Gaussian kernel with full width at half maximum of twice the voxel size.

140   *2.4.3 MRI data analysis*

141   The scans of the sham group were used to assess potential non-specific effects of SalB and its solvent

142   DMSO on the BOLD signal. Previous studies reported that SalB is an inactive metabolite of the KOR-

143   selective agonist Salvinorin A [26, 28]. However, DMSO has been shown to be able to modulate central

144   nervous system function [29]. To estimate this effect, we used the sham group that didn't express designer

145   receptors that could be affected by SalB/DMSO. Specifically, the BOLD signal from each voxel was

146   converted to percent signal change using the pre-injection baseline volumes (volumes 1-20) as a

147   reference. Then, the percent BOLD signal change across all sham animals were voxel-wise averaged to

148   create an average sham percent BOLD signal change scan. The resulting average percent BOLD signal

149   change timeseries showed a small linear signal drift before the injection (commonly observed drift in MRI

150   imaging), while after the injection an exponential-like decline indicated unspecific effects of SalB/DMSO.

151   These effects were fitted for each voxel by a linear fit with parameters a, b (volumes 5-20, given by

152   equation (1)) and a double exponential fit with parameters c, d, f and g (volumes 25-120, given by equation

153   (2)), which were connected at their crossing point to determine the final fitted curves (see Supplementary

154   figure 1):

$$\Delta S(t) = a \cdot t + b \qquad (1)$$

$$\Delta S(t) = c \cdot e^{d \cdot t} + f \cdot e^{g \cdot t} \qquad (2)$$

157   To identify the specific effects of the SalB injection in the KORD groups we calculated the differences

158   between the timeseries (percent signal change) of the KORD-expressing animals and the averaged sham

159   fits. To be certain that our fitting procedures closely reflected the BOLD activity in the sham group, we

160   only considered voxels with very high goodness of fit ($R^2 \geq 0.85$, Supplementary figure 1). Then, the area

161   under the curve (AUC) for the period starting at 10 min after SalB injection until 50 min post-injection

162   (volumes 40-120) was calculated in the KORD groups and used in further statistical analyses. For each SalB

163 concentration, mean statistical maps (one sample Student's T-test) were computed to test whether the

164 AUC values were statistically different from zero. In addition, a Paired Student's T-test was performed to

165 compare the effects of the two SalB concentrations in the KORD scan sessions. Next, regions of interest

166 (ROIs) were selected based on the Franklin and Paxinos mouse brain atlas (third edition) in various brain

167 regions, including: anterior cingulate area (ACA), retrosplenial cortex (RSP), insular cortex (Ins), visual

168 cortex (VIS), somatosensory cortex (SS), auditory cortex (AUD) / temporal association cortex (TEA),

169 amygdalar nuclei (AN) and hippocampus (HIP) (Supplementary Figure 2).

170 **2.5 Investigating KORD-induced functional connectivity changes**

171 *2.5.1 MRI data acquisition*

172 Resting state scans were acquired using a T_2^* weighted single shot EPI sequence (TR: 2000 ms, TE: 16 ms,

173 matrix: [128x64], FOV: (20x20) mm^2, in-plane resolution: (0.156x0.312) mm^2, 16 coronal slices of 0.4 mm

174 covering cerebrum excluding olfactory bulb). Two consecutive five-minute rsfMRI scans (150 volumes

175 each) were acquired starting ten minutes after the injection of either vehicle (DMSO) or SalB (3mg/kg).

176 The vehicle and SalB were used in MRI sessions. For the analysis, we selected the first of the two five-

177 minute scans unless excessive motion was observed, in which case the second scan was used (N=2). The

178 rsfMRI scans were acquired only in the KORD-expressing group.

179 *2.5.2 MRI data pre-processing*

180 The rsfMRI scans were pre-processed using SPM12 software in MATLAB2014a. Realignment was

181 performed using a least-squares approach and a 6-parameter rigid body spatial transformation. Further

182 pre-processing steps, consisting of normalization and smoothing, are analogous to the phMRI pre-

183 processing steps described above. The REST toolbox (REST 1.8, http://resting-fmri.sourceforge.net) was

184 used to filter the rsfMRI data. The band-pass filter was set between 0.01 and 0.1Hz to retain the low

185 frequency fluctuations of the BOLD signals.

2.5.3 MRI data analysis

Seed-based analyses were performed to assess FC alterations between brain regions that are known to

anatomically or functionally connect to the ACA. As such, seeds, consisting of 4 voxels, were drawn in the

ACA, RSP, Ins, VIS, SS, AUD/TEA, HIP and thalamus (Thal) for both hemispheres separately (Supplementary

Figure 3). The REST toolbox was used to obtain the mean BOLD signal time course of a seed region. Then,

this temporal signal was used in a general linear model analysis to compare it to the timecourse of all

other voxels in the brain. This resulted in a FC map consisting of voxels that significantly correlate with the

temporal signal of the seed region. Group mean FC maps were calculated for each seed region (One

sample Student's T-test). Masks were created consisting of the significant clusters of the mean group FC

maps of the vehicle scans and SalB scans (uncorrected p≤0.001, minimal cluster size = 10 voxels). The

masks of both scans were summed and these total masks were used in further analyses. Mean T-values

were extracted from the total masks. A Paired Student's T-test was used to compare the mean T-values

between both conditions. To assess interhemispheric FC, ROI time courses were extracted and Pearson's

correlation coefficients were calculated for each pair of ROIs. Then, the correlation values were z-

transformed and differences between the two conditions were assessed using a paired Student's T-test.

2.6 Whole-brain microscopy

2.6.1 Clearing and image acquisition

After the in vivo imaging procedures, brain samples were collected to evaluate KORD expression. Mice

were deeply anesthetized by an intraperitoneal injection with pentobarbital (Dolethal®, Vetoquinol,

Belgium). Cardiac perfusion, brain tissue preparation and clearing were done using the uDISCO protocol

[30]. Cleared mouse brains were recorded on an Ultramicroscope II (Lavision Biotec GmbH), equipped

with an Olympus MVPLAPO 2X (NA 0.50) objective lens and DBE-corrected LV OM DCC20 dipping cap.

Images were acquired with a Neo sCMOS camera (Andor) at 1.6X magnification and a 10μm z-step

9

209   resulting in a voxel size of 2 μm x 2 μm x 10 μm. Images acquired with left and right light sheet illumination

210   were merged with a linear blending algorithm. A 488nm (for EGFP and mCitrine) and 561nm laser (for

211   autofluorescence) with a 525/50nm and 620/60nm emission filters were used.

212   *2.6.2 Image analysis*

213   Regional analysis of the EGFP and mCitrine expression was done as previously described [31]. Briefly, the

214   autofluorescence channel was aligned to a 3D autofluorescence reference brain atlas (Allen Brain atlas)

215   using Elastix, and the resulting transformation vector was used for regional analysis of the fluorescent

216   protein signal [32]. To segment the fluorescent protein signal, a ratio image was generated by dividing the

217   signal channel by the autofluorescent channel in FIJI [33]. Edges were subsequently enhanced by applying

218   a Laplace filter (radius 75 μm), and binarized using a user-defined intensity threshold. Spurious signals

219   (e.g. at the contours of the brain, and edges within the tissue) were manually removed. Finally, the total

220   number of detected voxels for a given brain region volume was calculated and expressed relative to the

221   brain region size (Supplementary Figure 4).

222   **3.   Results**

223   Post-mortem whole-brain imaging after brain clearing (uDISCO) demonstrated that the targeted injection

224   site overlaps with the ACA region of the right hemisphere in both the sham group and the KORD-

225   expressing group (Supplementary Figure 4). Regional quantification of the mCitrine fluorescence showed

226   that significant signal from the KORD expression could only be observed in the target region. However,

227   similar injections of the EGFP control virus elicited stronger fluorescence that in addition to the target

228   region could also be observed in projecting regions, including motor and somatosensory regions,

229   retrosplenial cortex, insular cortex, thalamic nuclei and caudate putamen, with spreading to the

230   contralateral hemisphere.

10

231 **_3.1 Large scale network modulations upon KORD-induced neuronal inhibition in the right anterior_**

232 **_cingulate area_**

233 Pharmacological MRI was performed to assess in which brain regions the neural activity was modified

234 upon chemogenetic inhibition of the neurons in the right ACA. The mean statistical difference maps from

235 the comparison of both SalB concentrations in the KORD-expressing mice showed no significant clusters

236 (Paired Student's T-test, p≤0.005 uncorrected, minimal cluster size = 10 voxels). Therefore, the scans of

237 both conditions were grouped to evaluate the effect of SalB on the BOLD signal. Upon SalB injection, the

238 mean statistical AUC maps showed both significant BOLD signal decreases as well as increases (One

239 sample Student's T-test, p≤0.005, minimal cluster size = 10 voxels, Figure 1). Decreased BOLD signals were

240 observed as expected in the target region ACA, and in addition in Ins, left SS, left AUD/TEA and right VIS,

241 while, increased BOLD signals were observed in the right RSP, right SS, right HIP and AN. The mean AUC

242 values ± SEM from all voxels in the brain regions demonstrating significant decreases or increases (One

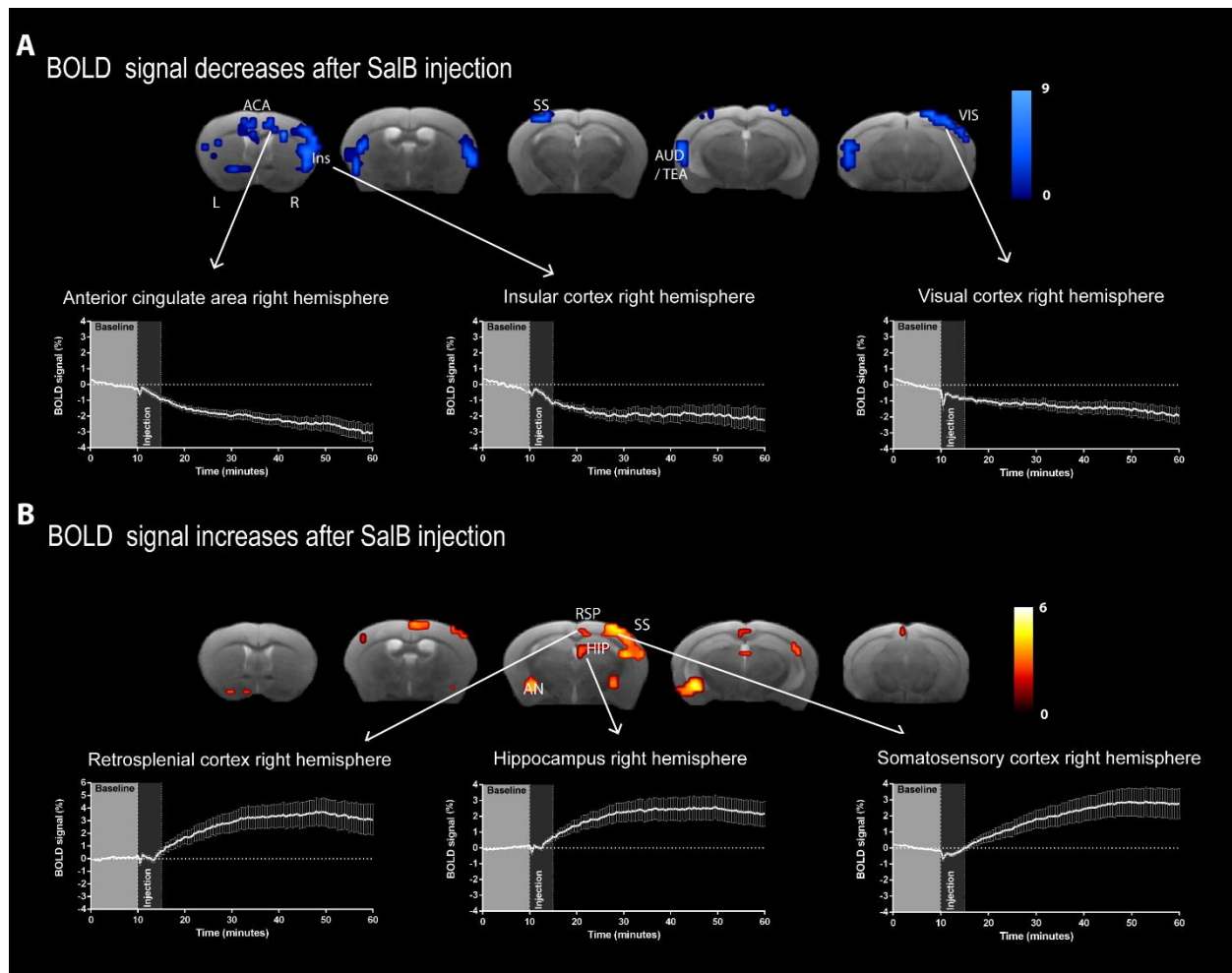243 sample Student's T-test) are presented in Table 1.

Figure 1. Neural activity alterations upon neuronal inhibition in right ACA. *Mean statistical AUC maps in the KORD-expressing group are shown. A) Mean statistical AUC maps of the significantly decreased BOLD signals after SalB injection. Graphs show the BOLD signal timeseries of all significant voxels in the right ACA, right Ins and right VIS. B) Mean statistical AUC maps of significantly increased BOLD signals after SalB injection. Graphs show the percent BOLD signal change timeseries of all significant voxels in the right RSP, right HIP and right SS. One sample T-test, p≤0.005, minimal cluster size = 10 voxels. Abbreviations: anterior cingulate area (ACA), insular cortex (Ins), auditory cortex (AUD), temporal association cortex (TEA), visual cortex (VIS), retrosplenial cortex (RSP), amygdalar nuclei (AN), somatosensory cortex (SS), hippocampus (HIP).*

12

Hemisphere	Brain region	Mean AUC ± SEM
Left hemisphere	Anterior cingulate area (ACA)	-1,3 ± 0,3
	Insular cortex (Ins)	-1,5 ± 0,4
	Somatosensory cortex (SS)	-1,5 ± 0,3
	Auditory cortex / temporal association cortex (AUD/TEA)	-2,1 ± 0,5
	Amygdalar nucleus (AN)	3,0 ± 0,8
Right hemisphere	Anterior cingulate area (ACA)	-1,2 ± 0,4
	Insular cortex (Ins)	-2,4 ± 0,5
	Somatosensory cortex (SS)	2,7 ± 0,7
	Hippocampus (HIP)	2,0 ± 0,7
	Retrosplenial cortex (RSP)	2,5 ± 0,8
	Visual cortex (VIS)	-1,4 ± 0,3
	Amygdalar nucleus (AN)	3,4 ± 1,0

Table 1. Quantification of the area under the curve (AUC). *Table shows the mean AUC ± SEM from the extracted timecourses of the significant voxels of different ROIs, including anterior cingulate area (ACA), insular cortex (Ins), somatosensory cortex (SS), auditory cortex (AUD) / temporal association cortex (TEA), hippocampus (HIP), retrosplenial cortex (RSP), visual cortex (VIS), amygdalar nucleus (AN).*

3.2 KORD-induced functional connectivity reductions

To evaluate how functional connectivity between different brain regions in changing during KORD-induced inactivation of the ACA, we analyzed the rsfMRI scans that were collected ten minutes after the injection of SalB. Seed-based analyses revealed that inhibition of the neurons in the right ACA significantly decreased FC of the right and left ACA, right and left RSP, right SS, right and left VIS, right AUD, left HIP and right and left Thal (Paired Student's T-test, Figure 2). Furthermore, interhemispheric FC was assessed between homologous ROIs in both hemispheres. Significantly decreased interhemispheric FC was measured for the RSP, SS and VIS (Paired Student's T-test, Figure 3).
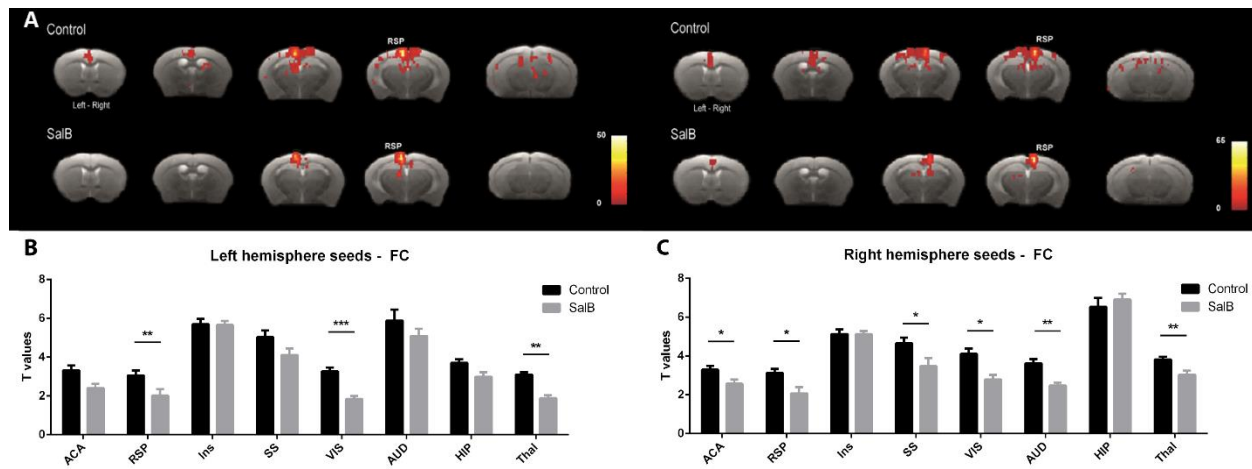
13

Figure 2. Functional connectivity alterations due to inhibition of the right ACA. *A) Statistical FC maps of the RSP as seed region after vehicle injection (control) and SalB injection (One sample T-test, p≤0.001 uncorrected, minimal cluster size 10 voxels). B + C) Bar graphs show the quantification of the mean T-values ± SEM, i.e. FC strength, for all seed regions (anterior cingulate area (ACA), retrosplenial cortex (RSP), insular cortex (Ins), visual cortex (VIS), somatosensory cortex (SS), auditory cortex (AUD), hippocampus (HIP) and thalamus (Thal); Paired Student's T-test). * p≤0.05, ** p≤0.01, *** p≤0.001.*
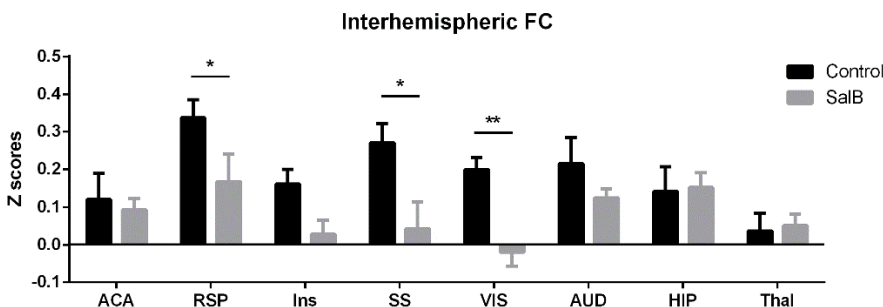

Figure 3. Inhibition of the right ACA induced decreased interhemispheric functional connectivity. *Bar graphs show mean Z-scores ± SEM of all brain regions (anterior cingulate area (ACA), retrosplenial cortex*

14

277 *(RSP), insular cortex (Ins), visual cortex (VIS), somatosensory cortex (SS), auditory cortex (AUD),*

278 *hippocampus (HIP) and thalamus (Thal); Paired Student's T-test). * p≤0.05, ** p≤0.01).*

3.3 Physiological parameters

280 To exclude potential physiological effects of SalB and/or DMSO injections. The breathing rate was

281 recorded during all *in vivo* imaging procedures. The breathing rates were compared across all groups to

282 evaluate whether observed neuronal activity and FC changes are influenced by alterations of the animals'

283 physiological condition. As such, breathing rates were compared between the sham-treated group and

284 the KORD-expressing group for the phMRI scans and between the two rsfMRI scan sessions, i.e. upon

285 vehicle injection and SalB injection, in the KORD-expressing group. The breathing rate in the sham group

286 (mean ± SEM: (155 ± 7) breaths per minute) did not significantly differ from the breathing rate of the

287 KORD-expressing mice (mean ± SEM: (160 ± 4) breaths per minute; two-sample Student's T-test, p=0.4).

288 Furthermore, the injected SalB concentration did not significantly influence the breathing rate in the KORD

289 – expressing mice (mean ± SEM (160 ± 4) breaths per minute with 3 mg/kg SalB injection and (165 ± 3)

290 breaths per minute with 6 mg/kg SalB injection; Paired Student's T-test p=0.4). In addition, no significant

291 difference could be observed in the breathing rate between the two rsfMRI scan sessions in the KORD-

292 expressing group (mean ± SEM: (157 ± 7) breaths per minute after vehicle injection and (158 ± 23) breaths

293 per minute after SalB injection; Paired Student's T-test, p=0.9).

4. Discussion

295 In this study, inhibitory chemogenetics were combined with non-invasive functional MRI to evaluate the

296 effects of neuronal inhibition in the ACA on whole-brain neuronal activity and FC. Inhibitory KORD were

297 expressed in the right ACA of mice, after which phMRI scans and rsfMRI scans were acquired. The phMRI

298 results showed that inhibition of the neurons in the right ACA induced BOLD signal decreases as well as

299 BOLD signal increases. Significantly decreased BOLD signals were observed in the target region, i.e. right

15

300   ACA, as well as in the left ACA, right and left INS, left SS, right VIS and left AUD. On the other hand,

301   increased BOLD signals were measured in the right SS, right and left AN, right RSP and right HIP. We further

302   hypothesized that inhibition can induce desynchronization of neuronal firing which can lead to disrupted

303   FC. Indeed, significantly decreased FC was observed for the ACA, RSP, SS, VIS, AUD and HIP. Histological

304   examination of the brains, using uDISCO clearing and light-sheet microscopy, revealed KORD expression

305   in the target region and structurally connected brain regions.

306   ***4.1 Neuronal inhibition of the right anterior cingulate area induced altered BOLD responses***

307   ***throughout the brain***

308   The KORD-induced inhibition of the right ACA caused significant modulations in the BOLD signals in the

309   ACA as well as inter-connected brain regions. A study has previously demonstrated that chemogenetic-

310   induced neural activity modulations could be observed using phMRI in the mesocorticolimbic system [24].

311   To the best of our knowledge, the study presented here shows for the first time whole-brain network

312   activity modulations upon the combined use of KORD-induced neuronal inhibition and phMRI in mice.

313   This approach allowed us to gain a better understanding of the importance of a preserved neuronal

314   activity in the ACA for whole-brain network activity and connectivity.

315   Although the exact function of the ACA is not yet fully known, several tracer injection studies have shown

316   its involvement in various networks. The ACA has been shown to mediate the transfer of information

317   between sensory areas, such as the somatosensory, visual and auditory cortices, and to higher order brain

318   regions including the prefrontal cortex [34]. This suggests that the ACA is implicated in movement

319   orientation and coordination of the eyes, head and body in object searching and spatial navigation. These

320   connections of the ACA with sensory regions could also be observed in our KORD-phMRI results. As such,

321   decreased BOLD signals were measured in the right visual cortex and left auditory cortex and increased

322   BOLD signals were observed in the right somatosensory cortex. Furthermore, it has been shown that the

16

323   ACA also receives information from the subiculum and transmits it to other prefrontal areas and it is

324   suggested to be part of a network supporting spatial orientation and episodic memory [4, 34].

325   Furthermore, previous tracer injection studies have shown that the ACA has reciprocal connections with

326   the retrosplenial cortex, visual cortex as well as with thalamic nuclei [35]. This is fully consistent with the

327   observed BOLD signal alterations in these brain regions after inhibition of the ACA in our study. However,

328   given that MRI is only an indirect measure of neuronal activity, and is unable to differentiate between

329   excitatory and inhibitory cell types, future research will be necessary in order to clarify the contributions

330   of specific cell classes in mediating the BOLD signal alterations.

331   ***4.2 Neuronal inhibition of the right anterior cingulate area induced whole-brain functional***

332   ***connectivity decreases***

333   In this study, rsfMRI showed decreased FC in different networks during inactivation of the ACA. Previous

334   human brain imaging studies used graph-theory based methods to identify a set of brain regions that play

335   a central role in the functional topology of the human brain. These regions include cingulate cortex, insular

336   cortex, frontal cortex, temporal cortex and the posterior cortex [36-38]. Similarly, Liska et al [39] found

337   high strength nodes in the mouse brain including the cingulate cortex and the prefrontal cortex. This might

338   explain the results in our study, as the inhibition of the ACA resulted in decreased FC in various brain

339   regions. By evaluating the FC of both unilateral and contralateral seeds, we could assess whether the

340   effect of KORD-mediated neuronal inhibition is localized in the ipsilateral, affected hemisphere or is also

341   spreading to the contralateral side. Our findings demonstrated FC alterations in both the ipsilateral and

342   contralateral hemisphere. We observed decreased FC for brain regions that are known to be structurally

343   connected with the ACA (see above). This is in line with the emerging view that functional correlations in

344   spontaneous brain activity are guided by underlying anatomical connections [14, 39]. The decreased FC

345   can thus be due to neuronal firing desynchronization mediated by disturbed inputs coming from the ACA.

346   We conjecture that the disruption of this hub region, with high connection strength and high degree of

347   structural connectivity, leads to widespread alterations in the integrity of the correlations between brain

348   networks and highlights the importance of hub node integrity in the dynamics of the whole network.

349   **5. Conclusion**

350   Our study demonstrates the ability of the combined use of KORD with *in vivo* MRI to assess large-scale

351   network activity and FC in response to inhibition of a hub region, namely the right ACA in the mouse brain.

352   We showed that KORD-induced inhibition of this area could induce BOLD signal decreases and increases

353   in connected brain regions throughout both hemispheres. The affected brain regions are in line with

354   previous tracer injection studies demonstrating projection areas of the ACA in mice. Furthermore, these

355   connected brain regions showed decreased FC measures. To conclude, our study identifies the DREADD

356   technology as a valuable and reliable tool that can be used in combination with non-invasive imaging

357   methods. This approach might be of significant value for future neuroscientific research trying to unravel

358   the underlying mechanisms of the function and dysfunction of neuronal networks.

363

364

365

366

367

References

1. Koike, H., M.P. Demars, J.A. Short, E.M. Nabel, S. Akbarian, M.G. Baxter, and H. Morishita, *Chemogenetic Inactivation of Dorsal Anterior Cingulate Cortex Neurons Disrupts Attentional Behavior in Mouse*, in *Neuropsychopharmacology*. 2016. p. 1014-23. DOI: 10.1038/npp.2015.229.

2. Diaz-Tejeiro, R., F. Maduell, J. Diez, N. Esparza, P. Errasti, A. Purroy, and J. Pardo, *Loss of renal graft due to recurrent IgA nephropathy with rapidly progressive course: an unusual clinical evolution*, in *Nephron*. 1990. p. 341-3. DOI: 10.1159/000185892.

3. Kim, J., E.A. Wasserman, L. Castro, and J.H. Freeman, *Anterior cingulate cortex inactivation impairs rodent visual selective attention and prospective memory*, in *Behav Neurosci*. 2016. p. 75-90. DOI: 10.1037/bne0000117.

4. Ding, H.K., C.M. Teixeira, and P.W. Frankland, *Inactivation of the anterior cingulate cortex blocks expression of remote, but not recent, conditioned taste aversion memory*, in *Learn Mem*. 2008. p. 290-3. DOI: 10.1101/lm.905008.

5. Weible, A.P., *Remembering to attend: the anterior cingulate cortex and remote memory*, in *Behav Brain Res*. 2013. p. 63-75. DOI: 10.1016/j.bbr.2013.02.010.

6. Paus, T., *Primate anterior cingulate cortex: where motor control, drive and cognition interface*, in *Nat Rev Neurosci*. 2001. p. 417-24. DOI: 10.1038/35077500.

7. Fuchs, P.N., Y.B. Peng, J.A. Boyette-Davis, and M.L. Uhelski, *The anterior cingulate cortex and pain processing*, in *Front Integr Neurosci*. 2014. p. 35. DOI: 10.3389/fnint.2014.00035.

8. Nordquist, R.E., C.M. Pennartz, H.B. Uylings, R.N. Joosten, A.J. Jonker, H.J. Groenewegen, and P. Voorn, *C-fos activation patterns in rat prefrontal cortex during acquisition of a cued classical conditioning task*, in *Behav Brain Res*. 2003. p. 65-75.

9. Vogt, B.A. and G. Paxinos, *Cytoarchitecture of mouse and rat cingulate cortex with human homologies*, in *Brain Struct Funct*. 2014. p. 185-92. DOI: 10.1007/s00429-012-0493-3.

10. Vogt, B.A., P.R. Hof, K. Zilles, L.J. Vogt, C. Herold, and N. Palomero-Gallagher, *Cingulate area 32 homologies in mouse, rat, macaque and human: cytoarchitecture and receptor architecture*, in *J Comp Neurol*. 2013. p. 4189-204. DOI: 10.1002/cne.23409.

11. Ma, Z., P. Perez, Z. Ma, Y. Liu, C. Hamilton, Z. Liang, and N. Zhang, *Functional atlas of the awake rat brain: A neuroimaging study of rat brain specialization and integration*, in *Neuroimage*. 2018. p. 95-112. DOI: 10.1016/j.neuroimage.2016.07.007.

12. Gozzi, A. and A.J. Schwarz, *Large-scale functional connectivity networks in the rodent brain*, in *Neuroimage*. 2016. p. 496-509. DOI: 10.1016/j.neuroimage.2015.12.017.

13. Sforazzini, F., A.J. Schwarz, A. Galbusera, A. Bifone, and A. Gozzi, *Distributed BOLD and CBV-weighted resting-state networks in the mouse brain*, in *Neuroimage*. 2014. p. 403-15. DOI: 10.1016/j.neuroimage.2013.09.050.

14. Risch, D., M. Castellote, C.W. Clark, G.E. Davis, P.J. Dugan, L.E. Hodge, A. Kumar, K. Lucke, D.K. Mellinger, S.L. Nieukirk, et al., *Seasonal migrations of North Atlantic minke whales: novel insights from large-scale passive acoustic monitoring networks*, in *Mov Ecol*. 2014. p. 24. DOI: 10.1186/s40462-014-0024-3.

15. Cao, Q., Y. Zang, L. Sun, M. Sui, X. Long, Q. Zou, and Y. Wang, *Abnormal neural activity in children with attention deficit hyperactivity disorder: a resting-state functional magnetic resonance imaging study*, in *Neuroreport*. 2006. p. 1033-6. DOI: 10.1097/01.wnr.0000224769.92454.5d.

16. Greicius, M., *Resting-state functional connectivity in neuropsychiatric disorders*, in *Curr Opin Neurol*. 2008. p. 424-30. DOI: 10.1097/WCO.0b013e328306f2c5.

414   17.   Boksman, K., J. Theberge, P. Williamson, D.J. Drost, A. Malla, M. Densmore, J. Takhar, W.
415   Pavlosky, R.S. Menon, and R.W. Neufeld, *A 4.0-T fMRI study of brain connectivity during word*
416   *fluency in first-episode schizophrenia*, in *Schizophr Res*. 2005. p. 247-63. DOI:
417   10.1016/j.schres.2004.09.025.
418   18.   Chepenik, L.G., M. Raffo, M. Hampson, C. Lacadie, F. Wang, M.M. Jones, B. Pittman, P.
419   Skudlarski, and H.P. Blumberg, *Functional connectivity between ventral prefrontal cortex and*
420   *amygdala at low frequency in the resting state in bipolar disorder*, in *Psychiatry Res*. 2010. p.
421   207-10. DOI: 10.1016/j.pscychresns.2010.04.002.
422   19.   Gai, Y., J. Zhao, L. Song, L. Wang, L. Qiu, X. Ning, X. Zheng, Y. Zhang, C. Mu, Y. Zhang, et al., *Two*
423   *thymosin-repeated molecules with structural and functional diversity coexist in Chinese mitten*
424   *crab Eriocheir sinensis*, in *Dev Comp Immunol*. 2009. p. 867-76. DOI: 10.1016/j.dci.2009.02.003.
425   20.   Hahn, A., P. Stein, C. Windischberger, A. Weissenbacher, C. Spindelegger, E. Moser, S. Kasper,
426   and R. Lanzenberger, *Reduced resting-state functional connectivity between amygdala and*
427   *orbitofrontal cortex in social anxiety disorder*, in *Neuroimage*. 2011. p. 881-9. DOI:
428   10.1016/j.neuroimage.2011.02.064.
429   21.   Bonnelle, V., R. Leech, K.M. Kinnunen, T.E. Ham, C.F. Beckmann, X. De Boissezon, R.J.
430   Greenwood, and D.J. Sharp, *Default mode network connectivity predicts sustained attention*
431   *deficits after traumatic brain injury*, in *J Neurosci*. 2011. p. 13442-51. DOI:
432   10.1523/JNEUROSCI.1163-11.2011.
433   22.   Mayer, A.R., M.V. Mannell, J. Ling, C. Gasparovic, and R.A. Yeo, *Functional connectivity in mild*
434   *traumatic brain injury*, in *Hum Brain Mapp*. 2011. p. 1825-35. DOI: 10.1002/hbm.21151.
435   23.   Giorgi, A., S. Migliarini, A. Galbusera, G. Maddaloni, M. Mereu, G. Margiani, M. Gritti, S. Landi, F.
436   Trovato, S.M. Bertozzi, et al., *Brain-wide Mapping of Endogenous Serotonergic Transmission via*
437   *Chemogenetic fMRI*, in *Cell Rep*. 2017. p. 910-918. DOI: 10.1016/j.celrep.2017.09.087.
438   24.   Roelofs, T.J.M., J.P.H. Verharen, G.A.F. van Tilborg, L. Boekhoudt, A. van der Toorn, J.W. de Jong,
439   M.C.M. Luijendijk, W.M. Otte, R.A.H. Adan, and R.M. Dijkhuizen, *A novel approach to map*
440   *induced activation of neuronal networks using chemogenetics and functional neuroimaging in*
441   *rats: A proof-of-concept study on the mesocorticolimbic system*, in *Neuroimage*. 2017. p. 109-
442   118. DOI: 10.1016/j.neuroimage.2017.05.021.
443   25.   Grayson, D.S., E. Bliss-Moreau, C.J. Machado, J. Bennett, K. Shen, K.A. Grant, D.A. Fair, and D.G.
444   Amaral, *The Rhesus Monkey Connectome Predicts Disrupted Functional Networks Resulting from*
445   *Pharmacogenetic Inactivation of the Amygdala*, in *Neuron*. 2016. p. 453-66. DOI:
446   10.1016/j.neuron.2016.06.005.
447   26.   Vardy, E., J.E. Robinson, C. Li, R.H.J. Olsen, J.F. DiBerto, P.M. Giguere, F.M. Sassano, X.P. Huang,
448   H. Zhu, D.J. Urban, et al., *A New DREADD Facilitates the Multiplexed Chemogenetic Interrogation*
449   *of Behavior*, in *Neuron*. 2015. p. 936-946. DOI: 10.1016/j.neuron.2015.03.065.
450   27.   Grandjean, J., A. Schroeter, I. Batata, and M. Rudin, *Optimization of anesthesia protocol for*
451   *resting-state fMRI in mice based on differential effects of anesthetics on functional connectivity*
452   *patterns*, in *Neuroimage*. 2014. p. 838-47. DOI: 10.1016/j.neuroimage.2014.08.043.
453   28.   Hooker, J.M., T.A. Munro, C. Beguin, D. Alexoff, C. Shea, Y. Xu, and B.M. Cohen, *Salvinorin A and*
454   *derivatives: protection from metabolism does not prolong short-term, whole-brain residence*, in
455   *Neuropharmacology*. 2009. p. 386-91. DOI: 10.1016/j.neuropharm.2009.06.044.
456   29.   Penazzi, L., J. Lorengel, F. Sundermann, N. Golovyashkina, S. Marre, C.M.B. Mathis, L.
457   Lewejohann, R. Brandt, and L. Bakota, *DMSO modulates CNS function in a preclinical Alzheimer's*
458   *disease model*, in *Neuropharmacology*. 2017. p. 434-444. DOI:
459   10.1016/j.neuropharm.2016.10.020.

460 30. Pan, C., R. Cai, F.P. Quacquarelli, A. Ghasemigharagoz, A. Lourbopoulos, P. Matryba, N. Plesnila,
461   M. Dichgans, F. Hellal, and A. Erturk, *Shrinkage-mediated imaging of entire organs and*
462   *organisms using uDISCO*, in *Nat Methods*. 2016. p. 859-67. DOI: 10.1038/nmeth.3964.
463 31. Detrez, J.R., H. Maurin, K. Van Kolen, R. Willems, J. Colombelli, B. Lechat, B. Roucourt, F. Van
464   Leuven, S. Baatout, P. Larsen, et al., *Regional vulnerability and spreading of*
465   *hyperphosphorylated tau in seeded mouse brain*, in *Neurobiol Dis*. 2019. p. 398-409. DOI:
466   10.1016/j.nbd.2019.03.010.
467 32. Klein, S., M. Staring, K. Murphy, M.A. Viergever, and J.P. Pluim, *elastix: a toolbox for intensity-*
468   *based medical image registration*, in *IEEE Trans Med Imaging*. 2010. p. 196-205. DOI:
469   10.1109/TMI.2009.2035616.
470 33. Zhao, B., K. Bhuripanyo, J. Schneider, K. Zhang, H. Schindelin, D. Boone, and J. Yin, *Specificity of*
471   *the E1-E2-E3 enzymatic cascade for ubiquitin C-terminal sequences identified by phage display*,
472   in *ACS Chem Biol*. 2012. p. 2027-35. DOI: 10.1021/cb300339p.
473 34. Zingg, B., H. Hintiryan, L. Gou, M.Y. Song, M. Bay, M.S. Bienkowski, N.N. Foster, S. Yamashita, I.
474   Bowman, A.W. Toga, et al., *Neural networks of the mouse neocortex*, in *Cell*. 2014. p. 1096-111.
475   DOI: 10.1016/j.cell.2014.02.023.
476 35. Zhang, S., M. Xu, W.C. Chang, C. Ma, J.P. Hoang Do, D. Jeong, T. Lei, J.L. Fan, and Y. Dan,
477   *Organization of long-range inputs and outputs of frontal cortex for top-down control*, in *Nat*
478   *Neurosci*. 2016. p. 1733-1742. DOI: 10.1038/nn.4417.
479 36. Cole, M.W., S. Pathak, and W. Schneider, *Identifying the brain's most globally connected regions*,
480   in *Neuroimage*. 2010. p. 3132-48. DOI: 10.1016/j.neuroimage.2009.11.001.
481 37. Sporns, O., *Network attributes for segregation and integration in the human brain*, in *Curr Opin*
482   *Neurobiol*. 2013. p. 162-71. DOI: 10.1016/j.conb.2012.11.015.
483 38. van den Heuvel, M.P. and O. Sporns, *Network hubs in the human brain*, in *Trends Cogn Sci*. 2013.
484   p. 683-96. DOI: 10.1016/j.tics.2013.09.012.
485 39. Liska, A., A. Galbusera, A.J. Schwarz, and A. Gozzi, *Functional connectivity hubs of the mouse*
486   *brain*, in *Neuroimage*. 2015. p. 281-91. DOI: 10.1016/j.neuroimage.2015.04.033.

487

488

489

490

491

492

493

494